Journal of Materials Chemistry A

ROYAL SOCIETY OF CHEMISTRY

PAPER

View Article Online
View Journal | View Issue

Cite this: J. Mater. Chem. A, 2023, 11, 14380

3D-structured bifunctional MXene paper electrodes for protection and activation of Al metal anodes†

Yeong Hoon Heo,‡[a] Juyun Lee,‡[bc] Son Ha,[a] Jong Chan Hyun,[a] Dong Hyuk Kang,[a] Juhee Yoon,[d] Hyun Soo Kim,[a] Yeonhua Choi,[a] Yun Chan Kang,[c] Hyoung-Joon Jin,[de] Seon Joon Kim *[bfg] and Young Soo Yun *[ah]

Received 28th March 2023
Accepted 1st June 2023

DOI: 10.1039/d3ta01840g

rsc.li/materials-a

Multivalent Al metal anodes (AMAs) can deliver high specific/volumetric capacities (2980 mA h g^{-1}/8046 mA h cm^{-3}) in chloroaluminate ionic liquid-based electrolytes (ILEs). However, strong corrosion of their surfaces and poor charge transfer kinetics in acidic ILEs remain critical obstacles to realizing high-performance AMAs. In this study, a 3D-structured bifunctional MXene paper electrode (3D-BMPE), which has distinctive material properties, such as high electrical conductivity, high elastic modulus, a large number of nanopores, and multitudinous oxygen functional groups, was fabricated to protect Al deposition/dissolution reactions with improved redox kinetics. The 3D-BMPE obstructed Al corrosion during the long rest time in the ILE and consecutive cycling process, resulting in a significantly stable cycling performance of the 3D-BMPE-based AMA over 2000 cycles. Furthermore, Al nucleation and growth reactions were catalyzed in the nanoporous structure surrounded by the highly functionalized MXene surfaces, which reduced overpotentials by one-sixth, resulting in highly improved coulombic efficiencies of ~99.9%. Moreover, the excellent electrochemical performance of the 3D-BMPE-based AMA was confirmed in Al-based dual-ion battery full cells, demonstrating the significant role played by 3D-BMPEs for AMAs.

Introduction

Rechargeable Al batteries (RABs) based on multivalent Al metal anodes (AMAs) are promising next-generation energy storage devices that can surpass current lithium-ion batteries in terms of both electrochemical performance and mass scalability owing to their high specific and volumetric capacity (2980 mA h g^{-1} and 8046 mA h cm^{-3}, respectively) and the abundance of Al resources.[1–3] However, sluggish ionic transfer on the surface of AMA caused by an oxide passivation layer has substantially impeded the commercialization of RABs.[4–9] Therefore, chloroaluminate ionic liquid-based electrolytes (ILEs) with high electrochemical stabilities have attracted considerable attention as an alternative for typical oxygen-containing organic electrolyte systems.[10,11] The ILE-based Al redox reaction follows a distinctive reaction mechanism that is based on anion redox chemistry, in which $4Al_2Cl_7^-$ can be reversibly transformed with $3e^-$ to Al^{3+} and $7AlCl_4^-$ during the charge/discharge process, as shown in eqn (1):

$$4Al_2Cl_7^- + 3e^- \rightarrow 7AlCl_4^- + Al \quad (1)$$

One of the key advantages of the ILE system is that the product $AlCl_4^-$ can be intercalated into graphitic lattices at a cathodic voltage range (~2 V *vs.* Al^{3+}/Al).[12–17] Because of their distinctive anion redox behavior, AMAs can be paired with inexpensive and stable graphite-based cathode hosts to form dual-ion redox systems.[18–20] Intensive research efforts have been devoted to developing Al-based dual ion batteries (Al-DIBs), with several studies reporting their considerable potential in high power density applications.[15,18,21–27] However, the insufficient

[a]KU-KIST Graduate School of Converging Science and Technology, Korea University, 145 Anam-ro, Seongbuk-gu, Seoul 02841, Republic of Korea
[b]Materials Architecturing Research Center, Korea Institute of Science and Technology, 5, Hwarang-ro 14-gil, Seongbuk-gu, Seoul 02792, Republic of Korea
[c]Department of Materials Science and Engineering, Korea University, 145, Anam-ro, Seongbuk-gu, Seoul 02841, Republic of Korea
[d]Program in Environmental and Polymer Engineering, Inha University, Incheon 22212, Republic of Korea
[e]Department of Polymer Science and Engineering, Inha University, Incheon 22212, Republic of Korea
[f]Division of Nanoscience and Technology, KIST School, University of Science and Technology, 5, Hwarang-ro 14-gil, Seongbuk-gu, Seoul 02792, Republic of Korea
[g]Convergence Research Center for Solutions to Electromagnetic Interference in Future-mobility, Korea Institute of Science and Technology, 5, Hwarang-ro 14-gil, Seongbuk-gu, Seoul 02792, Republic of Korea. E-mail: seonjkim@kist.re.kr
[h]Department of Integrative Energy Engineering, Korea University, 145, Anam-ro, Seongbuk-gu, Seoul 02841, Republic of Korea. E-mail: c-ysyun@korea.ac.kr

† Electronic supplementary information (ESI) available. See DOI: https://doi.org/10.1039/d3ta01840g

‡ These authors contributed equally to this work.

reaction kinetics of AMAs retard the charge storage kinetics of Al-DIBs, limiting their wide application prospects.[28] The AMA reaction kinetics are highly affected by the transfer rate of $Al_2Cl_7^-$ from the electrode surface because the local anion concentration sharply increases with the Al^{3+} reduction reaction.[29] Therefore, a stereoscopic electrode design aimed at a greater active surface area and improved product anion transfer rate is key to developing high-performance AMAs.[30,31] However, many challenges in using AMAs, such as large volume change, unexpected dendritic metal growth, and severe morphological changes caused by the Lewis acidic ILE, persist, which significantly deteriorates the electrochemical performances of Al-DIBs.[32–36] Particularly, the corrosive ILE seriously deforms the surface of AMA, resulting in non-uniform morphologies. No solution has yet been reported to prevent the active Al metal surface from undergoing severe morphological change.

MXenes are two-dimensional (2D) transition metal carbides and/or nitrides with the chemical formula $M_{n+1}X_nT_x$, where M is an early transition metal, X is carbon and/or nitrogen, n is an integer ranging from 1 to 4, and T_x represents surface functional groups.[41–43] MXenes can be a unique candidate as a catalytic electrode material to facilitate reversible phase transition reactions of Al ions owing to their high electrical conductivity coexisting with high-density surface functional groups that mainly comprise –OH, –O, and –F.[44–46] The high-density functional groups and the negatively charged surface have a high affinity toward Al ions, which can facilitate uniform Al metal nucleation and growth. Additionally, the excellent mechanical properties of MXenes enable them to function as a protective layer on the surface of AMAs by mitigating morphological changes and unexpected dendritic growth. Moreover, MXenes sheets can provide a significantly high surface area for Al redox reactions, owing to their high aspect ratio. However, 2D-like MXene sheets are prone to form a densely stacked morphology during assembly, leading to poor active surfaces, sluggish ionic transport kinetics, and insufficient electrolyte uptake ability. Thus, to effectively utilize catalytic MXene surfaces, designing a well-developed 3D MXene structure is essential; however, the development of a 3D-structured MXene electrode to realize high-performance AMAs has not yet been reported.

Herein, we synthesize a 3D-structured bifunctional MXene paper electrode (3D-BMPE) to protect and activate AMAs during Al deposition/dissolution cycles. The 3D-BMPE had a nanoporous structure surrounded by catalytically active sites for Al nucleation, in which Al redox reactions were induced without volume expansion or dendritic metal growth. More importantly, the 3D-BMPE served a protective function by significantly mitigating the galvanic-corrosion-induced degradation of electrochemical performance during long-term consecutive Al metal deposition/dissolution cycles, thus maintaining a high coulombic efficiency (CE) of ~99.9% and a highly stable cycling performance even after a long period of rest over several weeks. This result is in stark contrast to the severely degraded electrochemical performance of the reference AMA with no host electrode under galvanic corrosion. In addition, the extensively expanded active surface area reduces the effective current density, considerably improving the reaction kinetics of the intrinsically sluggish anion-based Al metal redox reactions. Furthermore, the significance of the versatile 3D-BMPE in AMAs was demonstrated through Al-DIB full-cell tests.

Experimental

Synthesis of $Ti_3C_2T_x$ MXene

Ti_3AlC_2 MAX powder (≤40 μm; Carbon-Ukraine) was used as a precursor to synthesize $Ti_3C_2T_x$ MXenes. Hydrochloric acid (HCl; 37%; Daejung) and lithium fluoride (LiF; 98.5%; Alfa Aesar) were used to synthesize the MAX etching solutions. Polystyrene nanospheres (PS NSs; 0.46 μm; Sigma-Aldrich) were used to synthesize porous $Ti_3C_2T_x$ MXene films. $Ti_3C_2T_x$ was synthesized by selective removal of Al etching from Ti_3AlC_2 using the MILD method.[47] First, 1.6 g of LiF was dissolved in 20 mL of aqueous 9 M HCl in a polypropylene bottle. Second, 1 g of Ti_3AlC_2 was slowly added to the solution with stirring to avoid an exothermic reaction. The etching process was carried out at 35 °C for 24 h. After the etching process was completed, the solution was repeatedly washed with deionized water (DI) until the pH reached 5–6. Finally, the delaminated $Ti_3C_2T_x$ MXene solution was obtained by performing centrifugation at 3500 rpm for 1 h and collecting the supernatant.

Synthesis of 3D-BMPE

First, 57.1 μL of 0.46 μm PS NSs and 50 mL of DI were mixed in a vial. Subsequently, 40 mg of $Ti_3C_2T_x$ was added to the solution and stirred with a magnetic bar for 2 h at room temperature. The aqueous solution was then vacuum-filtered to prepare the compact $Ti_3C_2T_x$-PS composite films. To obtain porous films, the composite films were annealed at 450 °C for 1 h under an Ar atmosphere to remove the PS NSs.

Characterization

The morphologies and microstructures of the samples were observed using field-emission scanning electron microscopy (FE-SEM; S-4300SE, Hitachi, Japan) and field-emission transmission electron microscopy (FE-TEM; JEM2100F, JEOL, Japan). The pore structure and specific surface areas of the samples were characterized using nitrogen adsorption–desorption isotherms (ASAP 2020, Micromeritics, USA) at −196 °C. The electrical conductivity and mechanical properties of the samples were characterized by conductometry (Loresta-GP MCP-T600, Mitsubishi Chemical, Japan) and nanoindentation (TI-950, Bruker), respectively. The microstructures of the samples were further analyzed using X-ray diffraction (XRD) patterns (D-max2500-PC, Rigaku, Japan; 40 kV, 200 mA, Cu Kα1 radiation, with $\lambda = 1.5406$ Å) in the 2θ range 3°–90°, with a scanning step of 0.02° and a scan speed of 2° min^{-1}, and Raman spectra (LabRAM HR Evolution, Horiba) with a laser of wavelength 785 nm. The surface chemical properties of the samples were investigated using X-ray photoelectron spectroscopy (XPS; PHI 5000 VersaProbe, ULVAC-PHI, Japan).

Electrochemical characterization

The electrochemical performance of 3D-BMPE was tested using a CR2032-type coin cell with an automatic battery cycler (WBCS3000, WonATech, South Korea). For the half-cell tests, the working electrode was fabricated by puncturing a stainless steel foil (10 μm; SS316L foil), 2D-MPE, and 3D-BMPE of diameter 1/2 inch. Al foils (0.25 mm; 99.999%, Sigma-Aldrich) were used as both counter and reference electrodes. The ILE was synthesized by mixing aluminum chloride ($AlCl_3$; 99.999%, anhydrous, powder, Sigma-Aldrich) and 1-ethyl-3-methylimidazolium chloride ([EMIM]Cl; ≥98%, across chemicals, previously heated in vacuum oven at 120 °C overnight, Sigma-Aldrich) at a 1.3 : 1.0 ratio in an Ar atmosphere. A glass microfiber filter (GF/F, Whatman) was used as a separator. The coin-cell assembly process was implemented in a glove box filled with Ar gas. For the symmetric cell tests, aluminum metal of 2 mA h cm^{-2} was electrochemically deposited on half-inch 2D-MPEs or 3D-BMPEs at 1 mA cm^{-2}, and then, two same Al/2D-MPEs or Al/3D-BMPEs were used as electrodes for the symmetric cells. For the Al-DIB full-cell tests, the cathode was prepared by mixing 90 wt% of commercial graphite powder (<20 μm, Sigma-Aldrich) and 10 wt% of polyvinylidene fluoride as active material and binder, respectively, through a slurry method, followed by coating on molybdenum foil (25 μm, 99.9%, Sigma-Aldrich) at a loading density of 3.5 mg cm^{-2}. Al metal was pre-deposited in different electrode systems of the AMA through half-cell systems with Al foil, and their Al-DIBs were assembled for full-cell tests. Electrochemical impedance spectroscopy (EIS) analysis was conducted in a frequency range from 0.1 Hz to 100 kHz using an iMPEdance analyzer (ZIVE SP2, WonATech, South Korea).

Results and discussion

A self-supporting 3D-BMPE was prepared through a simple template method using $Ti_3C_2T_x$ MXene and PS NSs *via* vacuum filtration, followed by thermal treatment (Fig. 1a and S1†). The FE-SEM images confirmed that it had a flat and uniform thickness of ∼25 μm and multitudinous nanopores that were well dispersed in the stereoscopic MXene matrix (Fig. 1b and c). To compare the effects of the 3D nanoporous structure on Al metal storage behavior, a non-porous MXene paper electrode (2D-MPE) was used as a control sample. It was fabricated in a similar way as the study samples but without using PS NSs. FE-SEM observation confirmed a densely packed MXene structure with poor nanopores (Fig. S2†). This indicates that the template method is effective for constructing nanoporous 3D-BMPEs. The nitrogen adsorption–desorption isotherm curves reveal a mesoporous structure of the 3D-BMPE, corresponding to IUPAC Type IV with an H3 hysteresis loop (Fig. 1d). The H3 pore is a slit-shaped mesopore that originates from the spaces between 2D-like MXene sheets. During the thermal treatment process, the PS NSs were emitted as flue gas upon decomposition. Rapid gas release can generate a broad range of mesopores in the 3D-BMPE structure. A similar mesoporous structure with an H3 hysteresis loop was also observed for the 2D-MPE. However, the specific pore volume of the 3D-BMPE (∼0.03 $cm^3\ g^{-1}$) was 25 times higher than that of the 2D-MPE (∼0.0012 $cm^3\ g^{-1}$). The negligible mesopore volume implies a more densely stacked microstructure of the 2D-MPE. For the macropores as observed in Fig. 1c, the macropore size distribution was analyzed by directly measuring the size of individual pores in multiple cross-sectional SEM images (Fig. S3†). The mean pore size was 0.46 μm, which corresponds to the PS NS that was initially added (Fig. S4†). The total pore volume was analyzed by calculating the difference in the film volume of 2D-MPE and 3D-BMPE, as it is reasonable to assume that the increased volume in 3D-BMPE is attributed to pores when the same amount of MXene is included. As a result, the pore volume of 3D-BMPE measured was 0.325 $cm^3\ g^{-1}$.

The presence of a large number of nanopores can result in an enhanced active electrochemical surface area (ECSA) for the Al redox reaction, which was confirmed through the cyclic voltammetry test conducted in the voltage range 0.01–0.7 V *vs.* Al^{3+}/Al (Fig. S5†). The ECSA of the 3D-BMPE calculated from the cyclic voltammogram was approximately 15 and 160 times that of the 2D-MPE and stainless steel foil electrode (SSE), respectively. Along with the positive effect on the active surface area, the nanopores had a slight negative effect on the electrical conductivity and mechanical properties. A four-probe-electrode measurement result revealed that the 3D-BMPE had a relatively lower electrical conductivity of $\sim 3.3 \times 10^3$ S cm^{-1} than the 2D-MPE ($\sim 7.8 \times 10^3$ S cm^{-1}) owing to voids induced by the numerous nanopores (Fig. 1e). Nevertheless, the electrical conductivity of the order of 10^3 S cm^{-1} is still very high, exceeding that of commercial conducting agents, such as carbon black ($\sim 10^2$ S cm^{-1}) and carbon nanotubes ($\sim 10^2$ S cm^{-1}).[37–40] A nanoindentation technique was employed to measure the mechanical properties of the MXene films. The elastic moduli of the 3D-BMPE and 2D-MPE were calculated to be 3.8 and 3.5 GPa, respectively, indicating that they both had good mechanical properties (Fig. 1e). The 3D-BMPE had slightly lower mechanical strength than the 2D-MPE owing to the presence of pores; however, they were at a comparable level.

XRD analysis was further conducted to investigate the interlayer structure of MXene layers. A sharp (002) peak at 8.14°, corresponding to a *d*-spacing of 1.09 nm, was mainly observed in the XRD pattern of the 3D-BMPE (Fig. 1f). The peak shapes and *d*-spacing values were similar to those of the 2D-MPE. Raman spectroscopy was conducted to confirm the surface terminations of the MXene building blocks (Fig. 1g). The Raman spectra of both 3D-BMPE and 2D-MPE show similar peaks at 119.7, 201.5, and 723.1 cm^{-1}, which coincide with those previously reported for $Ti_3C_2T_x$ functionalized with –OH, –O, and –F.[48] This result indicates that the MXene building blocks are of high quality with no oxidized species such as TiO_2. Moreover, the MXene building blocks of the 3D-BMPE have large numbers of O and F heteroatoms with high electronegativities, which was confirmed through XPS analysis (Fig. 1h–k). The Ti 2p region shows doublets of five deconvoluted peaks, with the $2p_{3/2}$ peaks centered at 455.0 eV (C–Ti^{+}–T_x), 456.0 eV (C–Ti^{2+}–T_x), 457.4 eV (C–Ti^{3+}–T_x), 458.9 eV (TiO_2), and 460.1 eV (C–Ti–F) (Fig. 1h).[44] The low-intensity peak of TiO_2 indicates

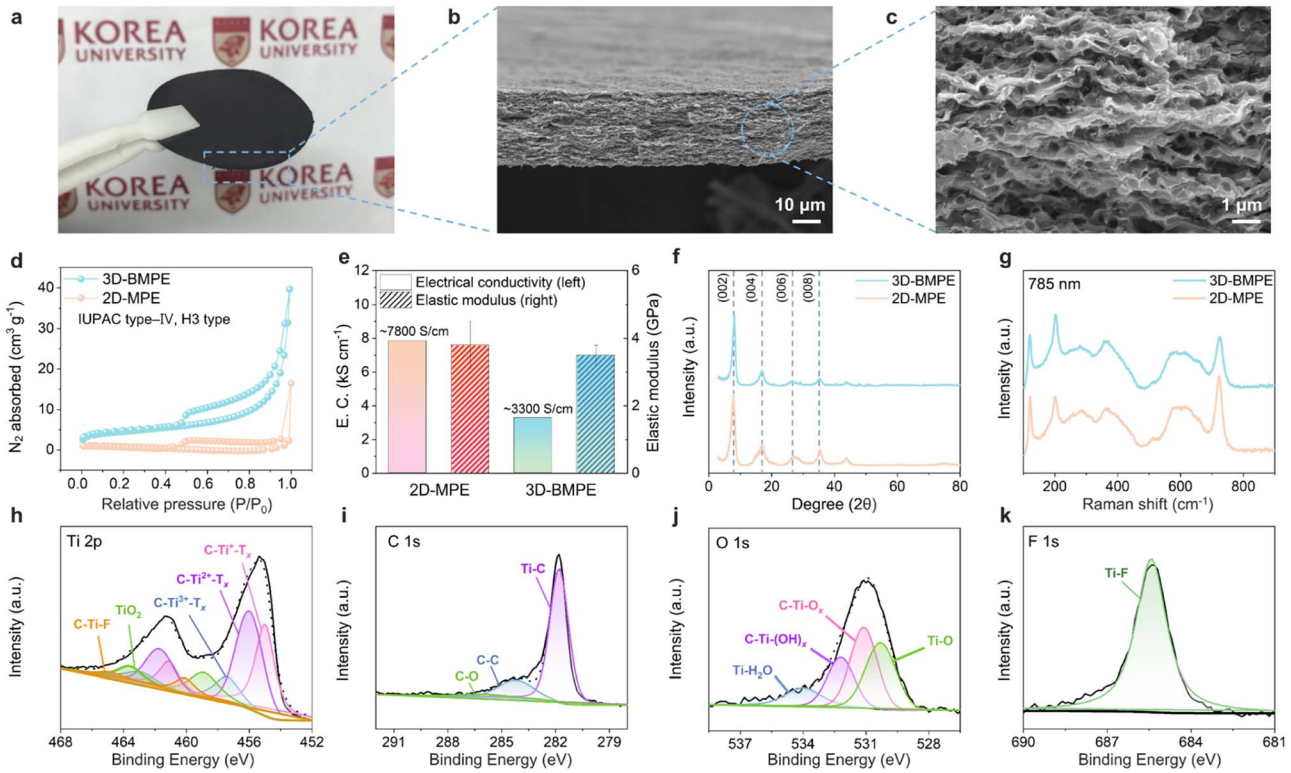

Fig. 1 Material properties of 3D-BMPE. (a) Optical and (b, c) FE-SEM images of 3D-BMPE at different magnifications; (d) nitrogen adsorption–desorption isotherm curves; (e) electric conductivity and elastic modulus; and (f) XRD patterns of 3D-BMPE and 2D-MPE. (g) Raman analyses of 3D-BMPE and 2D-MPE using a laser wavelength of 785 nm. Deconvoluted XPS (h) Ti 2p, (i) C 1s, (j) O 1s, and (k) F 1s spectra of 3D-BMPE.

a negligible degree of oxidation during the synthesis of 3D-BMPE, and the Ti–C peak arises from the conductive bonds within $Ti_3C_2T_x$ (Fig. 1i). The remaining peaks arise from covalent bonds that lead to the formation of surface functional groups. The O 1s region clearly shows the presence of oxygen functional groups with major deconvoluted peaks centered at 532.2 eV (C–Ti–$(OH)_x$) and 531.1 eV (C–Ti–O_x) (Fig. 1j).[44] Furthermore, the F 1s region shows the presence of fluorine functionalities in the form of Ti–F bonds at 685.1 eV (Fig. 1k).[44] The XPS peaks of the 3D-BMPE are highly similar to those of the 2D-MPE (Fig. S6†), indicating that the pore-synthesizing processes have a negligible influence on the surface properties of the MXene building blocks. The heteroatoms not only increased the electrolyte wettability and uptake ability, but also improved the Al nucleation kinetics, leading to preferential Al metal deposition/dissolution cycles in the nanopores. Hence, the 3D-BMPE possesses multiple properties that are key to activating and protecting Al redox reactions, such as extensive ECSA, multiple functional groups, well-developed nanopores, high electrical conductivity, and excellent mechanical properties.

The protective function of the 3D-BMPE was first confirmed through corrosive tests and electrochemical characterizations using both half and full cells (Fig. 2 and S7–S10†). The bare Al foil and 3D-BMPE with Al metal of 3 mA h cm^{-2} were immersed in the ILE solution for four weeks (referred to as "4-ILE"), and the changes in their morphologies and chemical properties were observed using FE-SEM and XPS, respectively. As shown in Fig. 2a and b, the flat surface of the bare Al foil became highly rough and messy. The optical images show a darkening of the bright bare Al surface (Fig. S7a and b†). The deconvoluted XPS Al 2p spectra reveal that the morphological change is related to the large increase in aluminum oxide because the relative peak ratio of Al–O bonding centered at ~74.8 eV to Al metal is significantly increased after four weeks in the ILE (Fig. 2g and S8a†).[49,50] The deconvoluted XPS O 1s spectra also reveal an increase in the relative intensity ratio of the aluminum oxide (~530.8 eV) to aluminum hydroxide (~531.8 eV) peaks (Fig. S9†).[50,51] These results indicate that the surface of the Al foil was corroded by the acidic ILE. Furthermore, after the 100th galvanostatic Al deposition/dissolution cycle of the Al foil that had been immersed in the ILE for four weeks (referred to as "100th-ILE"), the surface topologies were much more severely roughened (Fig. 2c and S7c†). Accordingly, the Al metal peak in the corresponding deconvoluted XPS Al 2p spectra almost completely disappeared after the cycling process (Fig. 2g). In contrast, the initial topology of the Al/3D-BMPE surface was well maintained after four weeks in the ILE (Fig. 2d, e, S7d and e†). The deconvoluted XPS Al 2p spectra indicate a larger Al metal to oxide peak ratio of Al/3D-BMPE after the long rest time in the ILE (Fig. 2h and S8b†). Although the surface topology of the Al/3D-BMPE was slightly changed after the 100th galvanostatic cycle, the degree of alteration was insignificant compared with that of the bare Al foil (Fig. 2f). The deconvoluted XPS Al 2p

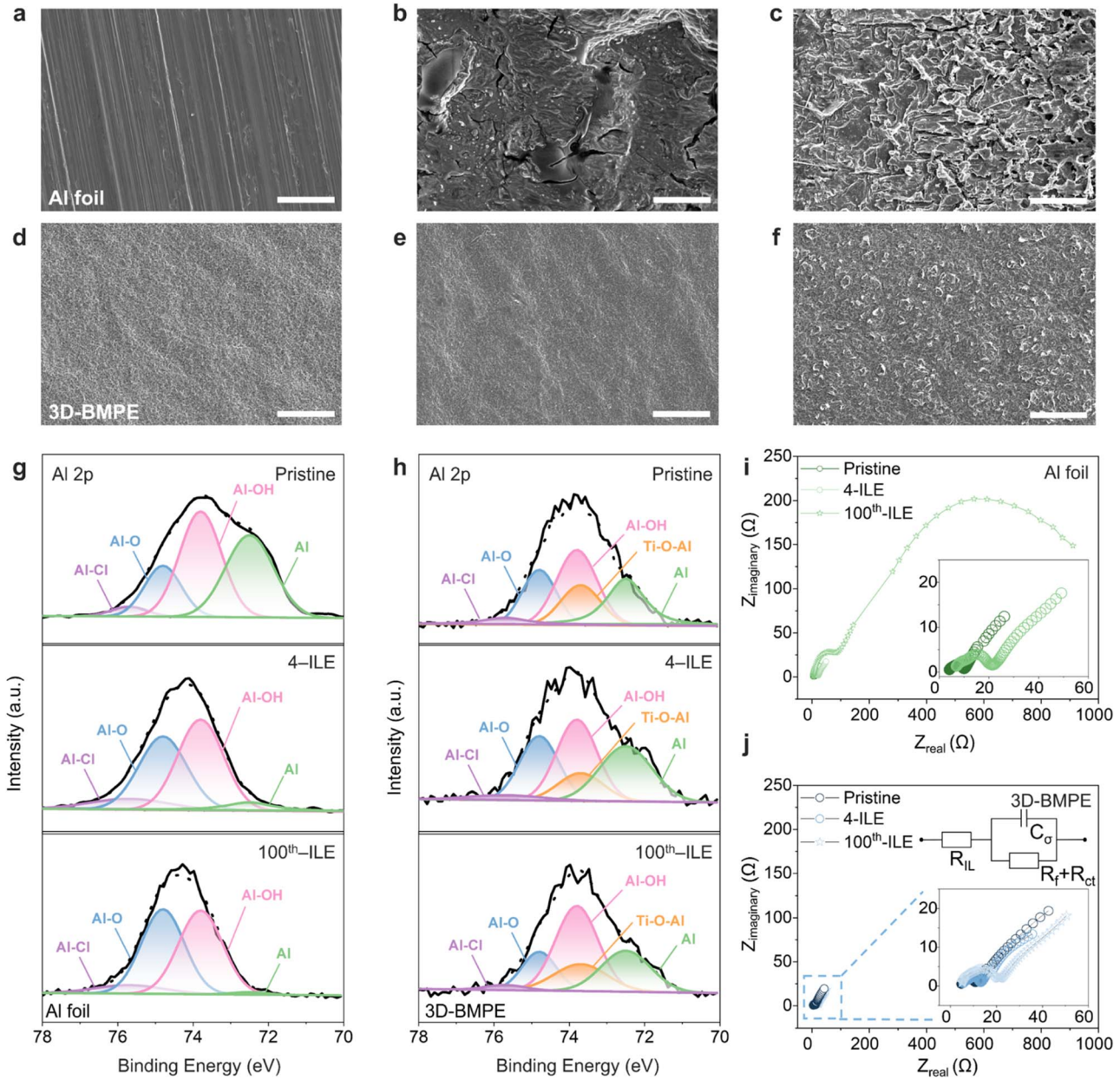

Fig. 2 Protective function of 3D-BMPE for AMA in the Lewis acidic ILE: FE-SEM images of (a) pristine Al foil, (b) Al foil after four weeks in ILE, (c) Al foil after 100th cycle, (d) pristine 3D-BMPE, (e) 3D-BMPE after four weeks in ILE, and (f) 3D-BMPE after 100th cycle; scale bar is 50 μm. Deconvoluted XPS Al 2p spectra of (g) Al foil and (h) 3D-BMPE and EIS profiles of (i) Al foil and (j) 3D-BMPE (inset of equivalent circuit model) at different experimental conditions.

spectra also show the presence of a clear Al metal peak after cycling, corroborating the result that Al metal corrosion is significantly mitigated by the 3D-structured MXene host structure (Fig. 2h). The deconvoluted XPS O 1s spectra reveal a slight change in the relative intensity ratio of the aluminum oxide to aluminum hydroxide peaks (Fig. S10†). Additionally, the protective effect of the 3D-BMPE was assessed using EIS (Fig. 2i and j). In the EIS profiles, a semicircle was observed in the high-frequency region, which represents a combination of the surface film resistance (R_f) and charge transfer resistance (R_{ct}). The semicircle of the bare Al foil corresponds to ~6 Ω, and a moderate upturn of ~15 Ω was observed after four weeks in the ILE (Fig. 2i). After the 100th cycle, the semicircle was split into two large semicircles, representing R_f and R_{ct}, which had multiple high values of >900 Ω (Fig. 2i). This means that most of the active surfaces were severely passivated by the aluminum oxide layers, and consequently, the Al redox reaction was significantly obstructed. In contrast, the semicircle in the EIS profile of the Al/3D-BMPE did not undergo any distinctive change (6–17 Ω) even after the 100th cycle, reaffirming the significant protective function of the MXene-based host structure (Fig. 2j). Hence, these results provide clear evidence that

3D-BMPEs can preserve AMAs from ILE-based galvanic corrosion during long rest times as well as the cycling process.

The electrochemical performance of the 3D-BMPE-based AMA was investigated at a cut-off capacity of 1 mA h cm^{-2} in the ILE at different areal current densities and compared with that of the 2D-MPE- and SSE-based AMAs. The half-cell tests were conducted using a handmade coin cell covered by a polymer sealing tape, except for a center hole where the working electrode is fixed (Fig. S11†). In the galvanostatic Al metal deposition process on the SSE at 0.1 mA cm^{-2}, a sharp negative voltage peak over −200 mV *vs.* Al^{3+}/Al was observed, and the voltage profile plateaued at −70 mV (Fig. 3a). The voltage gap between the peak point and plateau voltage is known as the nucleation overpotential (η_n), as shown in Fig. 3b. The large η_n value of ∼130 mV of the SSE can be decreased with catalytic electrode materials by reducing the free energy required for the phase-transition reaction (Fig. 3c). When the 2D-MPE was used for the Al metal nucleation reaction, η_n is significantly reduced by ∼19 mV (Fig. 3a). This result indicates the excellent catalytic effect of the functionalized MXene surfaces. Aluminum ions can be more strongly bound on the oxygen functional groups, leading to the lower η_n value. The catalytic effect is more pronounced in the 3D-BMPE, where η_n was further reduced by ∼14 mV (Fig. 3a). The η_n value of the 3D-BMPE is even lower than that in an aqueous electrolyte system.[52] In addition, the ohmic overpotential (η_o), which can be characterized by the voltage drop of the plateau section from the redox potential (Fig. S12†), was significantly reduced in the MXene-based substrate (Fig. 3a and b). The slight high η_o value of the 3D-BMPE is due to the reduction of electrical conductivity in the pore-generation process.

Another key observation from the Al deposition profiles for different electrode materials is the large gap in the concentration overpotential (η_c). η_c can be obtained from the plateau voltage variation at different states of charge (SoCs) (Fig. S12†). At different areal current densities from 0.1 to 2.0 mA cm^{-2}, the galvanostatic Al metal deposition/dissolution profiles show a gradual drop in voltage with increasing SoCs, which is more conspicuous at the higher areal current densities and SoCs (Fig. 3d–f). Particularly, at the areal current densities of 1.5 and 2.0 mA cm^{-2}, a dramatic decrease in voltage was confirmed at the higher SoCs for the SSE (Fig. 3d). Although the voltage drop is highly mitigated, it is still considerably large at higher areal current densities in the 2D-MPE (Fig. 3e). In contrast, the drop in voltage was significantly lower in the 3D-BMPE (Fig. 3f). These trends are clarified by the bar graphs depicting the total overpotentials (η_t) observed in the different electrode systems (Fig. 3g–i). The overpotentials of the SSE and 2D-MPE were approximately 600% and 200% higher than those of the 3D-BMPE, showing a sharp increase at the higher SoCs. In contrast, only a slight change in the overpotentials of the 3D-BMPE was observed even at higher areal current densities and SoCs, demonstrating the good charge transport performance of the 3D-BMPE. A close relationship between the total overpotentials and the average CE values was confirmed through cycling tests at different areal current densities (Fig. 3j). The high CE value (∼98.5%) of the SSE-based AMA at 0.5 mA cm^{-2} decreased significantly to 98.4, 97.5, and 95.2 with increasing areal current densities of 1.0, 1.5, and 2.0 mA cm^{-2}, respectively, whereas the CE of the 3D-BMPE-based AMAs was not only well maintained at the different areal current densities, but much higher on average (∼99.9%) at 1.5 and 2.0 mA cm^{-2}. In addition, the 3D-BMPE provided greater cycling stability and longer cycle life than the 2D-MPE and SSE (Fig. 3k). In galvanostatic Al metal deposition/dissolution cycles at 2.0 mA cm^{-2}, the 3D-BMPE-based AMA maintained stable discharge/charge cycling over 2000 cycles. In contrast, the SSE- and 2D-MPE-based AMAs showed poor cycling stabilities with large CE variations, with the cycling processes suddenly ending after just the 15th and 250th cycles for the SSE- and 2D-MPE-based AMAs, respectively. The cycling stabilities of the 2D-MPE- and 3D-BMPE-based AMAs were confirmed through symmetric cell tests (Fig. 3l). The galvanostatic profile of the 3D-BMPE-based AMA exhibited more stability and lower overpotentials over 2000 cycles, affirming its excellent cycling performance. The superior electrochemical performances of the 3D-BMPE-based AMAs compared with the previously reported results can be confirmed in Table S1.† The 3D-BMPE shows a relatively high CE value and better cycling stability. Moreover, the superiority of the 3D-BMPE-based AMA in cycling performances has been confirmed through a comparison cycling test in the similar electrochemical system with those of a redox-active multifunctional reduced graphene oxide-based AMA (Fig. S13†). The great electrochemical performances of the 3D-BMPE-based AMA are due to the versatile materials properties of the 3D-BMPE such as high electrical conductivity, high elastic modulus, a large number of nanopores, and multitudinous oxygen functional groups. Thus, the 3D-BMPE can be well-fitted as a host electrode for other multivalent metal storage such as magnesium, zinc, and calcium.

To demonstrate the feasibility of utilizing the high-performance 3D-BMPE-based AMA in Al-DIBs, full-cell tests were conducted using the Al/3D-BMPE anode with Al metal of 1 mA h cm^{-2} capacity and a commercial graphite cathode in the ILE system (Fig. S14†). The electrochemical performances of the Al/3D-BMPE//C_6 cells were compared with those of the reference full cells based on Al/SSE//C_6 and Al/2D-MPE//C_6. Handmade coin cells coated with a polymer sealing tape, except for the center hole, were used for the full-cell tests (Fig. S11†), and a Mo substrate was used as the cathode. In the Al/SSE//C_6 Al-DIBs, a reversible capacity of ∼41 mA h g^{-1} was obtained at 0.1 A g^{-1} (Fig. 4a). The reversible capacity was significantly decreased by <10 mA h g^{-1} on increasing the current density to ≥0.3 A g^{-1}, indicating their poor rate capabilities. This could be attributed to the large overpotentials of the SSE-based AMA induced by surface corrosion and sluggish Al redox kinetic performance. When the 2D-MPE was introduced in the AMA, the reversible capacity of the Al/2D-MPE//C_6 cells increased to ∼74 mA h g^{-1} at 0.1 A g^{-1}. At higher current densities of 0.3, 0.5, 0.8, and 1.0 A g^{-1}, they showed much better capacity retention, corresponding to 67, 54, 46, and 40 mA h g^{-1}, respectively (Fig. 4b). In comparison, the 3D-BMPE-based AMA in the Al/3D-BMPE//C_6 cells led to a further increase in the reversible capacity to ∼79 mA h g^{-1} and higher rate capabilities than those

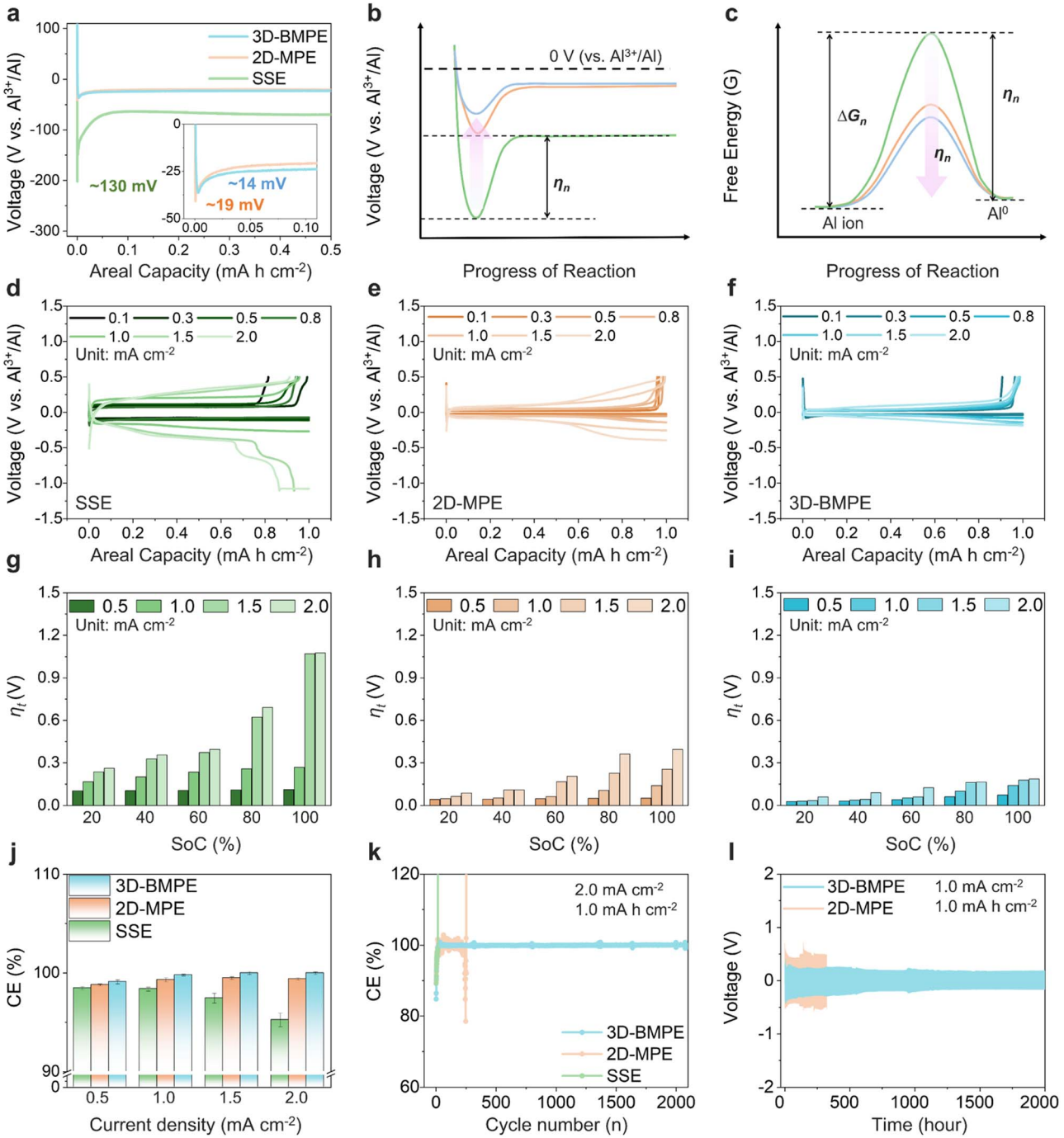

Fig. 3 Electrochemical performances of SSE, 2D-MPE, and 3D-BMPE: (a) galvanostatic aluminum deposition profiles at 0.1 mA cm^{-2}; plots showing (b) nucleation overpotential and (c) catalytic effect for aluminum nucleation reaction. Galvanostatic aluminum deposition/dissolution profiles at different areal current densities on (d) SSE, (e) 2D-MPE, and (f) 3D-BMPE. Bar graphs showing the total overpotentials of (g) SSE, (h) 2D-MPE, and (i) 3D-BMPE at different SoCs. (j) CE values at different areal current densities. Cycling performances of (k) SSE, 2D-MPE, and 3D-BMPE at half-cell configurations, and (l) 2D-MPE and 3D-BMPE at symmetric cell configurations.

of the 2D-MPE-based AMA (Fig. 4c). Even at 1.0 A g^{-1}, the Al-DIBs based on Al/3D-BMPE//C_6 retained a capacity of ~64 m A h g^{-1}. These results suggest that the SSE-based AMA is a rate-determining factor for Al/SSE//C_6 cells, and the electrochemical performance of Al-DIBs can be significantly improved by introducing a 3D-structured catalytic electrode material. In addition to offering better kinetics, the 2D- and 3D-BMPE-based Al-DIB systems fully recovered to their respective initial capacities when the current density returned to its initial value after 100 consecutive cycles, demonstrating their good reversibility (Fig. 4d). Even in the 2D-MPE-based Al-DIBs, the higher reversible capacity similar to that of 3D-BMPE-based Al-DIBs

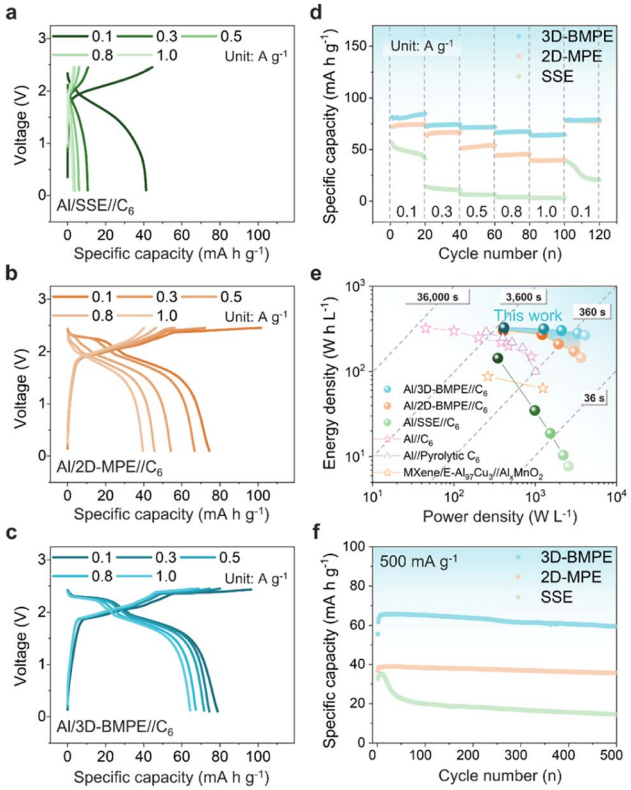

Fig. 4 Electrochemical performances of the different Al-DIBs, namely Al/SSE//C_6, Al/2D-MPE//C_6, and Al/3D-BMPE//C_6: galvanostatic aluminum deposition/dissolution profiles of (a) Al/SSE//C_6, (b) Al/2D-MPE//C_6, and (c) Al/3D-BMPE//C_6 at different areal current densities; (d) rate capabilities, (e) Ragone plots, and (f) cycling performances of the Al-DIBs.

was achieved after 100 cycles at different current densities. This capacity improvement is due to a gradual increase of active surface area with a repetitive cycling process in the well-stacked MXene electrode. Ragone plots showed the specific energy and power relationships of the different Al-DIB full cells (Fig. 4e). Although the same Al active anode materials are used for Al-DIBs, the energy and power densities are substantially affected by the catalytic host electrodes. The Al/SSE//C_6 cells had an energy density of ~3.4 W h kg^{-1} at ~1128.3 W kg^{-1}, whereas the Al/2D-MPE//C_6 and Al/3D-BMPE//C_6 cells had energy densities of ~63.3 W h kg^{-1} at ~1599.5 W kg^{-1} and ~115.7 W h kg^{-1} at ~1797.2 W kg^{-1}, respectively. The tenfold higher energy density of the Al/3D-BMPE//C_6 cells at the higher power density indicates the benefit of using 3D-structured catalytic electrode materials in AMAs. Considering densities of Al/3D-BMPE and C_6, the volumetric energy density of Al/3D-BMPE//C_6 cells is ~264.79 W h L^{-1}. This value is much higher than those of the previously reported aluminum-based energy storage devices.[12,53,54] Moreover, the cycling stabilities of the Al/2D-MPE//C_6 and Al/3D-BMPE//C_6 cells were well maintained over 500 cycles, whereas the Al/SSE//C_6 cells showed a drastic capacity drop after a few cycles (Fig. 4f). The initial capacity decay could be attributed mainly to the surface corrosion of AMA in the acidic ILE system. The contrasting cycling performance revealed that the host structure composed of rigid MXene building blocks successfully protected the AMA during the long cycling process, leading to a feasible cycling performance. Hence, despite using the same Al active anode material, large differences in electrochemical performances were observed according to the host electrode materials in Al-DIBs, which clearly indicates that the protective Al redox strategy using catalytic 3D-BMPEs is invaluable for Al-DIBs.

Conclusions

Existing AMAs in ILE-based Al-DIBs show inadequate electrochemical performance because of surface corrosion and large overpotentials, leading to poor cycling and rate performances. This obstacle can be overcome by introducing a 3D catalytic host electrode based on functionalized MXene building blocks. A 3D-BMPE with distinctive mechanical, electrical, and chemical properties can activate and protect Al redox reactions in the nanoporous structure, leading to highly stable and long cycling over 2000 cycles and excellent rate capabilities with high average CE values of 99.9% at 2.0 mA cm^{-2}. In addition, the 3D-BMPE-based Al-DIB exhibited >10 times higher energy density (~1797.2 W h kg^{-1}) and more stable cycling performance over 500 cycles than the one based on the 2D-MPE. This result suggests that a catalytic host electrode for an AMA is key to achieving high-performance Al-DIBs and that 3D-BMPE can be a suitable candidate.

Author contributions

Conceptualization: YHH, JL, SJK, YSY, Investigation: YHH, JL, JY, HSK, YC, formal analysis: HYH, SH, JCH, DHK, project administration: SH, JCH, DHK, SJK, YSY, supervision: JY, YCK, H-JJ, Validation: YHH, JL, HSK, visualization: YHH, JL, SH, DHK, writing-original draft: YHH, JL, writing-review & editing: SJK, YSY.

Conflicts of interest

There are no conflicts to declare.

Acknowledgements

The authors acknowledge Sookyung Huh for her contribution to MXene synthesis. This research was supported by a National Research Foundation of Korea (NRF) grant (2021R1C1C1006385), funded by the Ministry of Science and ICT (MSIT). This research was supported by a National Research Council of Science & Technology (NST) grant from the Korean government (MSIT) (CRC22031-000). This work was supported by the KU-KIST School Program. This research was supported by the Basic Science Research Program of the National Research Foundation of Korea (NRF), funded by the Ministry of Education (NRF-2019R1A2C1084836 and NRF-2021R1A4A2001403).

Notes and references

1 D. Larcher and J. M. Tarascon, *Nat. Chem.*, 2015, **7**, 19–29.
2 G. A. Elia, K. Marquardt, K. Hoeppner, S. Fantini, F. Lin, E. Knipping, W. Peter, J.-F. Drillet, S. Passerini and R. Hahn, *Adv. Mater.*, 2016, **28**, 7564–7579.
3 K. L. Ng, B. Amrithraj and G. Azimi, *Joule*, 2022, **6**, 134–170.
4 N. R. Levy, M. Auinat and Y. Ein-Eli, *Energy Storage Materials*, 2018, **15**, 465–474.
5 X. Zhang and T. M. Devine, *J. Electrochem. Soc.*, 2006, **153**(9), B375.
6 Y. Matsuda, Y. Ouchi and H. Tamura, *J. Appl. Electrochem.*, 1974, 53–56.
7 H. Wang, S. Gu, Y. Bai, S. Chen, B. Zhu, C. Wu and F. Wu, *J. Mater. Chem. A*, 2015, **3**, 22677–22686.
8 H. He, H. Tong, X. Song, X. Song and J. Liu, *J. Mater. Chem. A*, 2020, **8**, 7836–7846.
9 H. Wang, S. Gu, Y. Bai, S. Chen, F. Wu and C. Wu, *ACS Appl. Mater. Interfaces*, 2016, **8**, 27444–27448.
10 J. S. Wilkes, J. A. Levisky, F. A. Wilson and C. L. Hussey, *Inorg. Chem.*, 1982, **21**(3), 1263–1264.
11 N. Jayaprakash, S. K. Das and L. A. Archer, *Chem. Commun.*, 2011, **47**, 12610–12612.
12 M. C. Lin, M. Gong, B. Lu, Y. Wu, D.-Y. Wnag, M. Guan, M. Angell, C. Chen, J. Yang, B.-J. Hwang and H. Dai, *Nature*, 2015, **520**, 324–328.
13 L. Wang, X. Song, T. Hu, W. Yan, Z. Tie and Z. Jin, *Energy Storage Materials*, 2022, **44**, 461–468.
14 A. S. Childress, P. Parajuli, J. Zhu, R. Podila and A. M. Rao, *Nano Energy*, 2017, **39**, 69–76.
15 D. Y. Wang, C. Y. Wei, M. C. Lin, C. J. Pan, H. L. Chou, H. A. Chen, M. Gong, Y. Wu, C. Yuan, M. Angell, Y. J. Hsieh, Y. H. Chen, C. Y. Wen, C. W. Chen, B. J. Hwang, C. C. Chen and H. Dai, *Nat. Commun.*, 2017, 14283.
16 C. J. Pan, C. Yuan, G. Zhu, Q. Zhang, C. J. Huang, M. C. Lin, M. Angell, B. J. Hwang, P. Kaghazchi and H. Dai, *Proc. Natl. Acad. Sci. U. S. A.*, 2018, **115**(22), 5670–5675.
17 G. A. Elia, G. Greco, P. H. Kamm, F. Garcia-Moreno, S. Raoux and R. Hahn, *Adv. Funct. Mater.*, 2020, **30**, 2003913.
18 X. Zhang, T. Tang, F. Zhang and C. S. Lee, *Adv. Energy Mater.*, 2016, **6**, 1502588.
19 S. Wang, K. V. Kravchyk, A. N. Filippin, U. Muller, A. N. Tiwari, S. Buecheler, M. I. Bodnarchuk and M. V. Kovalenko, *Adv. Sci.*, 2018, **5**, 1700712.
20 S. Wnag, S. Jiao, W. L. Song, H. S. Chen, J. Tu, D. Tian, H. Jiao, C. Fu and D. N. Fang, *Energy Storage Materials*, 2018, **12**, 119–127.
21 H. Chen, H. Xu, S. Wang, T. Huang, J. Xi, S. Cai, F. Guo, Z. Xu, W. Gao and C. Gao, *Sci. Adv.*, 2017, **3**(12), eaao7233.
22 Z. Liu, J. Wang, H. Ding, S. Chen, X. Yu and B. Lu, *ACS Nano*, 2018, **12**, 8456–8466.
23 X. Tong, F. Zhang, G. Chen, X. Liu, L. Gu and Y. Tang, *Adv. Energy Mater.*, 2018, **8**, 1701967.
24 L. Zhang, L. Chen, H. Luo, X. Zhou and Z. Liu, *Adv. Energy Mater.*, 2017, **7**, 1700034.
25 X. Yu, B. Wang, D. Gong, Z. Xu and B. Lu, *Adv. Mater.*, 2017, **29**, 1604118.
26 L. L. Chen, W. L. Song, N. Li, H. Jiao, X. Han, Y. Luo, M. Wang, H. Chen, S. Jiao and D. Fang, *Adv. Mater.*, 2020, **32**, 2001212.
27 Y. Kong, C. Tang, X. Huang, A. K. Nanjundan, J. Zou, A. Du and C. Yu, *Adv. Funct. Mater.*, 2021, **31**, 2010569.
28 S. Ha, J. C. Hyun, J. H. Kwak, H. D. Lim, B. S. Youn, S. Cho, S. H. J. Jin, H. K. Lim, S. M. Lee and Y. S. Yun, *Chem. Eng. J.*, 2022, 135416.
29 J. Yoon, S. Moon, S. Ha, H. K. Lim, H. J. Jin and Y. S. Yun, *J. Energy Chem.*, 2022, **74**, 121–127.
30 J. Li, K. S. Huii, S. Ji, C. Zha, C. Yuan, S. Wu, F. Bin, X. Fan, F. Chen, Z. Shao and K. N. Hui, *Carbon Energy*, 2022, **4**, 155–169.
31 Q. Zhao, J. Zheng, Y. Deng and L. Archer, *J. Mater. Chem. A*, 2020, **8**, 23231–23238.
32 H. Chen, H. Xu, B. Zheng, S. Wang, T. Huang, F. Guo, W. Gao and C. Gao, *ACS Appl. Mater. Interfaces*, 2017, **9**, 22628–22634.
33 Y. Long, H. Li, M. Ye, Z. Chen, Z. Wang, Y. Tao, Z. Weng, S. Z. Qiao and Q. B. Yang, *Energy Storage Materials*, 2021, **34**, 194–202.
34 M. Zhang, J. S. Watson, R. M. Counce, P. C. Trulove and T. A. Zawodrinski Jr, *J. Electrochem. Soc.*, 2014, **161**(4), D161–D167.
35 J. Zheng, D. C. Bock, T. Tang, Q. Zhao, J. Yin, K. R. Tallman, G. Wheeler, X. Liu, Y. Deng, S. Jin, A. C. Marschilok, E. S. Takeuchi, K. J. Takeuchi and L. A. Archer, *Nat. Energy*, 2021, **6**, 398–406.
36 N. Lindahl, J. Bitenc, R. Dominko and P. Johansson, *Adv. Funct. Mater.*, 2020, **30**, 2004573.
37 D. Pantea, H. Darmstadt, S. Kaliaguine, L. Summchen and C. Roy, *Carbon*, 2001, **39**, 1147–1158.
38 M. E. Spahr, R. Gilardi and D. Bonacchi, *Carbon Black for Electrically Conductive Polymer Applications*, Springer International Publishing, 2017.
39 G. Chen, D. N. Futaba, S. Sakurai, M. Yumura and K. Hata, *Carbon*, 2014, 318–325.
40 L. Zhang, G. Zhang, C. Liu and S. Fan, *Nano Lett.*, 2012, **12**, 4848–4852.
41 B. Anasori, M. R. Lukatskaya and Y. Gogotsi, *Nat. Rev. Mater.*, 2017, **2**, 16098.
42 X. Li, Z. Huang, C. E. Shuck, G. Liang, Y. Gogotsi and C. Zhi, *Nat. Rev. Chem.*, 2022, **6**, 389–404.
43 A. VahidMohammadi, J. Rosen and Y. Gogotsi, *Science*, 2021, **372**, eabf1581.
44 S. Ha, D. Kim, H. K. Lim, C. M. Koo, S. J. Kim and Y. S. Yun, *Adv. Funct. Mater.*, 2021, **31**, 2170328.
45 S. J. Kim, H. J. Koh, C. E. Ren, O. Kwon, K. Maleski, S. Y. Cho, H. Anasori, C. K. Kim, Y. K. Choi, J. Kim, Y. Gogotsi and H. T. Jung, *ACS Nano*, 2018, **12**, 986–993.
46 J. L. Hart, K. Hantanasirisakul, A. C. Lang, B. Anasori, D. Pinto, T. Pivak, J. T. Omme, S. J. May, Y. Gogotsi and M. L. Taheri, *Nat. Commun.*, 2019, **10**, 522.
47 M. Alhabeb, K. Maleski, B. Anasori, P. Lelyukh, I. Clark, S. Sin and Y. Gogotsi, *Chem. Mater.*, 2017, **29**, 7633–7644.

48 A. Sarycheva and Y. Gogotsi, *Chem. Mater.*, 2020, **32**, 3480–3488.
49 T. T. Luong, B. T. Tran, Y. T. Ho, T. W. Wei, Y. H. Wu, T. C. Yen, L. L. Wei, J. S. Maa and E. Y. Chang, *Electron. Mater. Lett.*, 2015, **11**(3), 352–359.
50 F. Wu, N. Zhu, Y. Bai, Y. Gao and C. Wu, *Green Energy Environ.*, 2018, 71–77.
51 A. H. Alshehri, K. Mistry, V. H. Nguyen, K. H. Ibrahim, D. Munoz-Rogjas, M. Yavuz and K. P. Musselman, *Adv. Funct. Mater.*, 2019, **29**, 1805533.
52 H. Ma, H. Chen, B. Yang, J. Feng, Y. Xu, Y. Sun, H. Cheng, C. Li, X. Yan and L. Qu, *Energy Environ. Sci.*, 2022, **15**, 1131–1143.
53 N. P. Stadie, S. Wang, K. V. Kravchyk and M. V. Kovalenko, *ACS Nano*, 2017, **11**, 1911–1919.
54 Q. Ran, S. Zeng, M. Zhu, W. Wan, H. Meng, H. Shi, Z. Wen, X. Lang and Q. Jiang, *Adv. Funct. Mater.*, 2023, **33**, 2211271.